

On the irradiation tolerance of nano-grained Ni-Mo-Cr alloy: 1MeV He⁺ irradiation experiment

Zhenbo Zhu^{1,2}, Hefei Huang^{1,2*}, Ondrej Muránsky^{3,4}, Jizhao Liu^{1,2}, Zhiyong Zhu^{1,2}, Yi Huang^{5,6}

¹ Shanghai Institute of Applied Physics, Chinese Academy of Sciences, Shanghai 201800, China

² School of Nuclear Science and Technology, University of Chinese Academy of Sciences, Beijing 100049, China

³ Australian Nuclear Science and Technology Organisation (ANSTO), Lucas Heights, Sydney, NSW, 2234, Australia

⁴ University of New South Wales (UNSW), Kensington, Sydney, NSW, 2052, Australia

⁵ Department of Design and Engineering, Faculty of Science and Technology, Bournemouth University, Poole, Dorset BH12 5BB, UK

⁶ Materials Research Group, Department of Mechanical Engineering, University of Southampton, Southampton SO17 1BJ, UK

Abstract

The irradiation damage behavior was studied in the nano-grained Ni-Mo-Cr alloy (nano-grained GH3535), which was irradiated by He ion to various dose. The evolution of defects and hardness changes are characterized by transmission electron microscopy and nanoindentation to explore the irradiation tolerance of the nano-grained GH3535 and the coarse-grained GH3535 (annealed GH3535), where the later was chosen as reference material to make comparison with nano-grained GH3535. The results show that though both the average size and number density of He bubbles increase with an increase in the irradiation dose, the smaller volume fraction is found in the nano-grained GH3535 compared with the coarse-grained GH3535 under the same irradiation condition. This indicates that the nano-grained GH3535 possess better irradiation swelling resistance than the coarse-grained GH3535. However, the increase in the hardness of the nano-grained GH3535 is more significant than in the coarse-grained GH3535 under the same irradiation dose. This suggests stronger irradiation-induced hardening of the nano-grained alloy comparing to coarse-grained alloy, due to the impeding effect caused by grain boundaries decorated with He bubbles. This study provides insight into the design of irradiation-tolerant nickel-based alloys for nuclear industry applications.

Keywords: Nano-grained nickel-based alloys; He ion irradiation; He bubble; Swelling; Irradiation induced hardening.

Corresponding author: Hefei Huang (huanghefei@sinap.ac.cn)

1. Introduction

Molten salt reactors (MSRs) are one of the six most promising advanced Generation IV nuclear systems [1]. To date, since nickel-based alloy UNS N10003 alloy (Hastelloy N alloy, GH3535 alloy) have excellent resistant to molten fluoride salt, it been widely accepted as the most promising candidate structural materials [2, 3]. However, the dimensional instability produced by neutron irradiation has been a cause of much concern in terms of safety and structural integrity. Point defects introduced by energetic neutron aggregate to form vacancy clusters, dislocation loops and solute cluster. Additionally, He bubble produced by the (n,α) transmutation reaction of nickel with neutrons can precipitate into He bubbles because of its low solubility [4]. These defects result in irradiation-induced hardening, He embrittlement and swelling, thus degrade the mechanical properties and threaten safety of reactor. For nickel-based alloys, it has been found that He embrittlement is the primary irradiation degradation pathway [5].

The development of irradiation resistance materials is a critical issue for a longer and safer cycle in nuclear reactors. Introducing high-density nanoscale defect sinks, such as grain boundaries [6], nanoprecipitates [7] and free surface [8, 9], is an appealing strategy to eliminate irradiation-induced point defects and alleviate the degradation of mechanical properties. Because of their improved mechanical properties [10], nano-grained materials have been received great attention and extensively studied in recent years. Several experimental and theoretical studies on nano-grained materials have been done and found that nano-grained materials with increased grain boundary population are more tolerant to high radiation doses compared with traditional materials [10-16]. Several severe plastic deformation (SPD) techniques, such as ball milling, high-pressure torsion (HPT), equal-channel angular pressing (ECAP) etc. have been used to fabricate nano-grained alloys [17]. Additionally, these techniques can produce materials with unique combinations of properties, such as extraordinarily high strength and ductility, high fatigue life and toughness [18]. However, rare investigation on the irradiation resistance of nano-grained alloy fabricated by SPD has been reported.

Due to the advantages of nano-grained structure developed from SPD techniques, the nano-grained GH3535 alloy fabricated by HPT was chosen to verify their effectiveness in obstructing He swelling and irradiation induced hardening. Additionally, defects evolution, such as He bubbles and loops in nano-grained materials with grain size smaller than 100 nm have rarely been studied. Since the grain size has influence on the resistance tolerant to irradiation [19-21], the smaller grain size may influence the behavior of He bubble and dislocation loops differently. Thus, these defects behavior in the nano-grained GH3535 could be explored.

In this work, the nano-grained GH3535 was irradiated using high energy He ions, with the coarse-grained GH3535 (annealed GH3535) as reference materials. The evolutions of microstructure and mechanical property degradation of nano-grained GH3535 are systematically investigated. The purpose of this study is to study the resistance tolerance of the nano-grained GH3535 and assist in the development of irradiation resistant nickel-based alloy.

2. Experimental

A Ni-Mo-Cr alloy (GH3535), with compositions shown in Table 1 [22], was co-developed by Institute of Metal Research (IMR), and Shanghai Institute of Applied Physics (SINAP) of the Chinese Academy of Science as the molten-salt-facing material in proposed MSR systems. The GH3535 alloy

is typically used in the fully solution-annealed condition with coarse-grain microstructure, which is referred to as norm-GH3535 hereafter. The EBSD orientation map in Fig. 1(a) reveals its bimodal microstructure consisting of coarse ($> 50 \mu\text{m}$) and fine ($< 50 \mu\text{m}$) equiaxed grains with a large number of annealing twins and about 1.25% of Mo-rich $M_6[\text{C}, \text{Si}]$ complex carbides. In order to apply HPT, we cut disk samples (10 mm in diameter and 0.8 mm in thickness) from the as-received fully-annealed plate so that the disk normal was parallel to the rolling direction (RD) of the plate. Disk samples were then subjected to HPT processing to produce nano-grained microstructure [23]. HPT processing was conducted at room temperature with a pressure of 6.0 GPa and rotation speed of 1 rpm. GH3535 disk samples were processed up to 10 turns by HPT. As shown in Fig. 1(b), the nano-grained GH3535 (referred to as nano-GH3535 hereafter) has rather equiaxed grains while the grain size analysis shown in Fig. 1(c) suggests the average grain size of about 70 nm.

Table 1. The nominal chemical composition (in wt. %) of GH3535 alloy

Elements	Ni	Mo	Cr	Fe	Mn Si C Al Cu
wt. %	Bal.	17.1	7.1	4.2	< 1.5

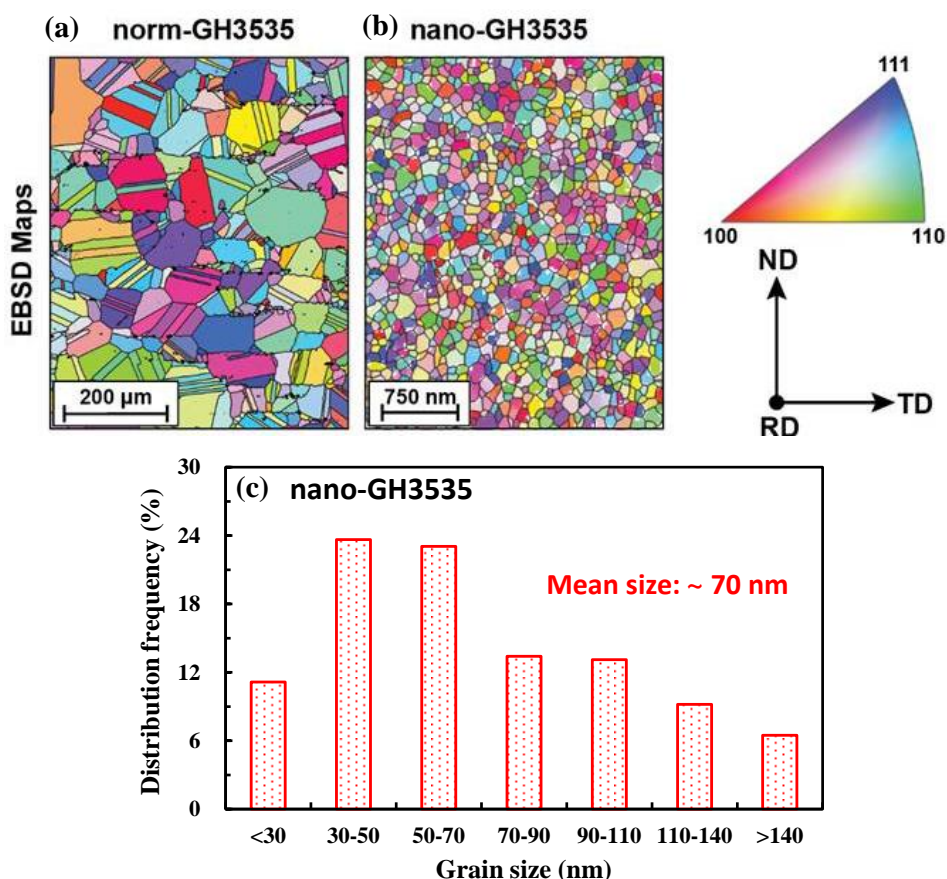


Fig. 1. EBSD orientation maps of (a) norm-GH3535, (b) nano-GH3535 and (c) the grain size distribution of nano-GH3535.

In order to explore the effect of the nano-grained microstructure on the irradiation, we have irradiated both norm-GH3535 and nano-GH3535 alloys. Samples for ion irradiation were first mechanically polished to a mirror-like finish before being further electro-polished to remove any

surface stresses. The polished samples were then irradiated at 650 °C using 1MeV He⁺ ions to fluences of 1×10^{16} , 3×10^{16} and 6×10^{16} ions/cm² for about 1, 3 and 6 hours. Fig. 2 presents SRIM [24] predictions of He concentration and displacement-per-atom (dpa) as a function of depth (distance from the irradiated surface) for the ion fluence of the 3×10^{16} ions/cm² – the He concentration reaches a peak value of ~1.4 at. % at depth of ~1700 nm, which also roughly coincides with the maximum dpa damage. In the present SRIM calculations, we used displacement threshold energy of 40 eV for Ni, Fe and Cr elements and 60 eV for Mo. These are the main alloying elements in GH3535 alloy (Table 1), whereas minor alloys elements were omitted from the calculation. Furthermore, one need to keep in mind that the SRIM calculations do not take into account the state of microstructure, hence, the SRIM predictions are identical for both norm-GH3535 and nano-GH3535 alloy.

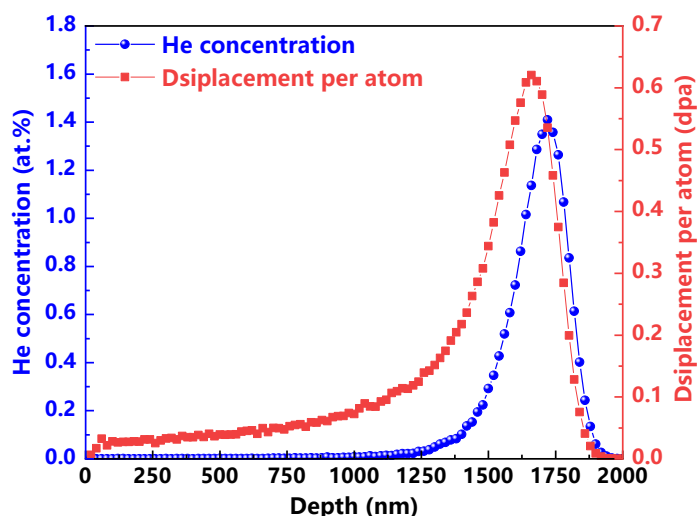


Fig. 2. The depth distribution of He concentration and displacement per atom in GH3535 with He ion fluence of 3×10^{16} ions/cm².

Following the ion beam irradiation, we examined the He bubbles formation and the effect of their presence on mechanical properties (i.e. irradiation-induced hardening) of both coarse-grained and nano-grained GH3535 alloys. The distribution and size of formed He bubbles was examined using TEM after extracting a cross-sectional sample about 50 nm in thickness employing the Ga⁺-based FIB. This was done employing Tecnai G2 F20 Transmission Electron Microscopy (TEM), and Helios G4 UX Focused Ion Beam (FIB). Here, the final milling was performed with Ga beam energy of 5 KeV at a current of about 8 pA to avoid the sample damage caused by Ga ions during sample preparation. The effect of formed He bubbles on mechanical properties of the alloys was then explored using nano-indentation measurements employing G200 nano-indenter. A diamond Berkovich tip with a radius of 20 nm was used with the continuous stiffness measurement (CSM) method and the maximum penetration depth was set 1200 nm. Twelve independent indents were made at each depth – i.e. the distance from the irradiation surface – we then found the mean (average) and standard deviation of obtained measurements as a function of depth.

3. Results and discussion

It is well-understood that the high-energy particle irradiation leads to the formation of vacancies and interstitials, which are generated as a result of displacement cascade [25, 26]. These point defects

can (i) recombine and annihilate, (ii) aggregate into point-defects clusters, or (iii) get trapped by so-called defect sinks such as grain boundaries, dislocations, present interphases, etc. However, since interstitials in metals diffuse generally faster than vacancies [27, 28], they might reach grain boundaries faster leaving behind mobile vacancies [20]. These then agglomerate to form vacancy clusters, which then hinder the motion of dislocations leading to the irradiation-induced hardening. When it comes to He atoms they can get trapped at grain boundaries or dislocations to form He bubbles. However, they can get also trapped by formed vacancy clusters leading to formation of He-vacancy complexes [29], which then act as a nucleus site for He bubbles. Formed He bubbles cause the irradiation-induced swelling, and similarly to the vacancy clusters they interact with moving dislocation leading to the irradiation-induced hardening [30-32]. This is caused by the interaction between the stress fields associated with irradiation-induced defects (bubbles, clusters, etc.), and stress fields of moving dislocations [20]. In what follows, we first discuss the effect of the state of the microstructure on the He bubbles formation and irradiation-induced swelling, and then we look into their effect on the mechanical properties and the irradiation-induced hardening.

3.1 Effect of the grain size on the He bubbles formation

In the present work, we employed TEM to survey the number density, size, shape and distribution of the formed He bubbles as a function of depth – i.e. the distance from the irradiated surface. Fig. 3(a) presents collected TEM images in the vicinity of the peak damage. The SRIM calculation shown in Fig. 2 suggests that maximum peak damage and maximum He concentration is expected in the depth of about 1750 to 1950 nm. The predictions of the SRIM calculations are confirmed in Fig. 3(a), where the number density of formed He bubbles is presented as bar chart. It then becomes clear from Fig. 3(b-d) that He bubbles are distributed heterogeneously with preferential nucleation along the grain boundary (yellow arrows). There is, however, a fair amount of He bubbles still present within grains – these presumably nucleate from the formed vacancy clusters or presents dislocations found within grains. Furthermore, as one would expect the TEM analysis revealed that both the size and number density of He bubbles increases with an increasing fluence (irradiation dose).

As regards the shape of observed bubbles, we found that He bubbles along the gain boundaries have somewhat ellipsoidal shape when irradiated to the highest fluence of 6×10^{16} ions/cm². This can be explained by their growth along the grain boundaries. It is, further, noted that the size of He bubbles along the grain boundaries is not evidently larger than those found within grains. The detail analysis of collected TEM images focused on the distribution, density and the size of formed He bubbles is then shown in Fig. 4. Note that the count shown in Fig. 4 includes He bubbles found in the intergranular regions as well as grain boundaries. Since some of the observed helium bubbles are elliptical, the long axis dimension is selected as the representative size of the bubbles in this study. Fig. 4(a) suggests an increasing size of the formed He bubbles with an increasing ion fluence from about 1.48, 1.98 to 2.29 nm. Interestingly, under the current elevated temperature irradiation conditions, no irradiation-induced dislocation loops or precipitation in irradiated nano-GH3535 were observed. The absence of dislocation loops is presumably a consequence of high-density of effective defect sinks such as a large amount of grain boundaries found in nano-grained microstructure [20].

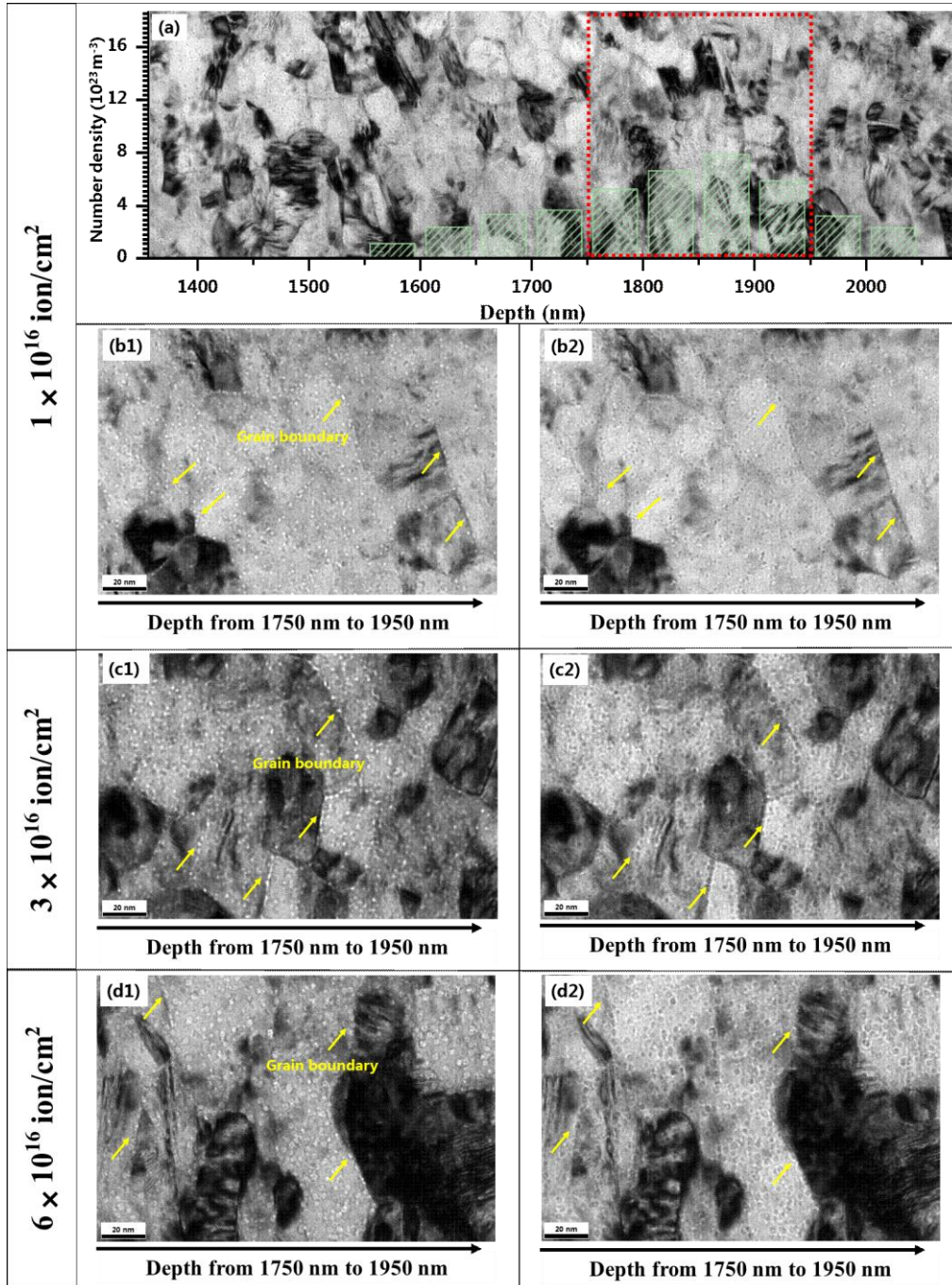


Fig. 3. (a) The bright-field TEM micrograph of the post-irradiated nano-GH3535 (650 °C, 1×10^{16} ions/cm²) superimposed with the number density of the formed He bubbles. (b-d) The magnified images of peak damage regions under under-focus and over-focus conditions of all examined fluences.

In order to evaluate the effect of the formation of He bubbles on irradiation-induced swelling, we further obtained the volume fraction ($\frac{V_1}{V_2}$) of He bubbles, the ratio of the total volume of helium bubbles (V_1) to that of the sample (detected region) (V_2), from present TEM analysis using following relationship [10]:

$$\frac{V_1}{V_2} = \frac{4}{3}\pi r^3 N_d, \quad (1)$$

where r and N_d are the equivalent radius and number density of the He bubbles, respectively. It is important to note that this method of estimating volume fraction of formed He bubbles ignores the influence of small bubbles since only bubbles observable in TEM are included [10]. The resultant volume fraction of He bubbles was estimated to be 0.035%, 0.098% and 0.182% for the nano-GH3535 irradiated to fluences of 1×10^{16} , 3×10^{16} , 6×10^{16} ions/cm², respectively.

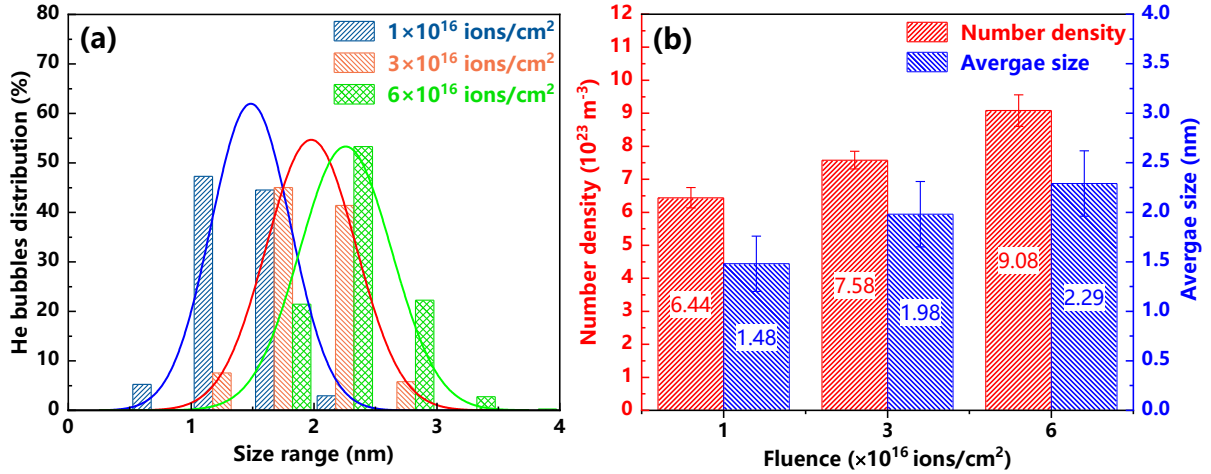


Fig. 4. (a) The He bubbles size distribution in the peak damage region for all examined fluences and (b) corresponding He bubble number density and their average size.

In order to assess the resistance to He bubble formation (swelling) of the nano-GH3535, the identical irradiation condition are repeated on the norm-GH3535 – He⁺ irradiation at 650 °C to a fluence of 3×10^{16} ions/cm². Fig. 5(a) shows the typical TEM bright field under-focus image superimposed with the obtained distribution of He bubbles. It is clear that the He bubbles are found in the depth from about 1110 nm to 2100 nm. The black dot-like features in Fig. 5(a) in the depth of 600-2100 nm are dislocation loops or/and solute clusters, which were reported in Ref. [30, 33]. The micrographs at the peak damage region (1750 nm - 1950 nm, Fig. 2) are obtained under the under-focus and over-focus conditions, which are shown in Figs. 5(b) and 5(c). Compared with the nano-GH3535, He bubbles are evenly distributed in the matrix of norm-GH3535 and have more-or-less identical size. The number density, average size and volume fraction are also calculated, and corresponding values are 6.36×10^{23} m⁻³, 2.39 nm and 0.145% – these agrees well with the previous study in Ref. [30].

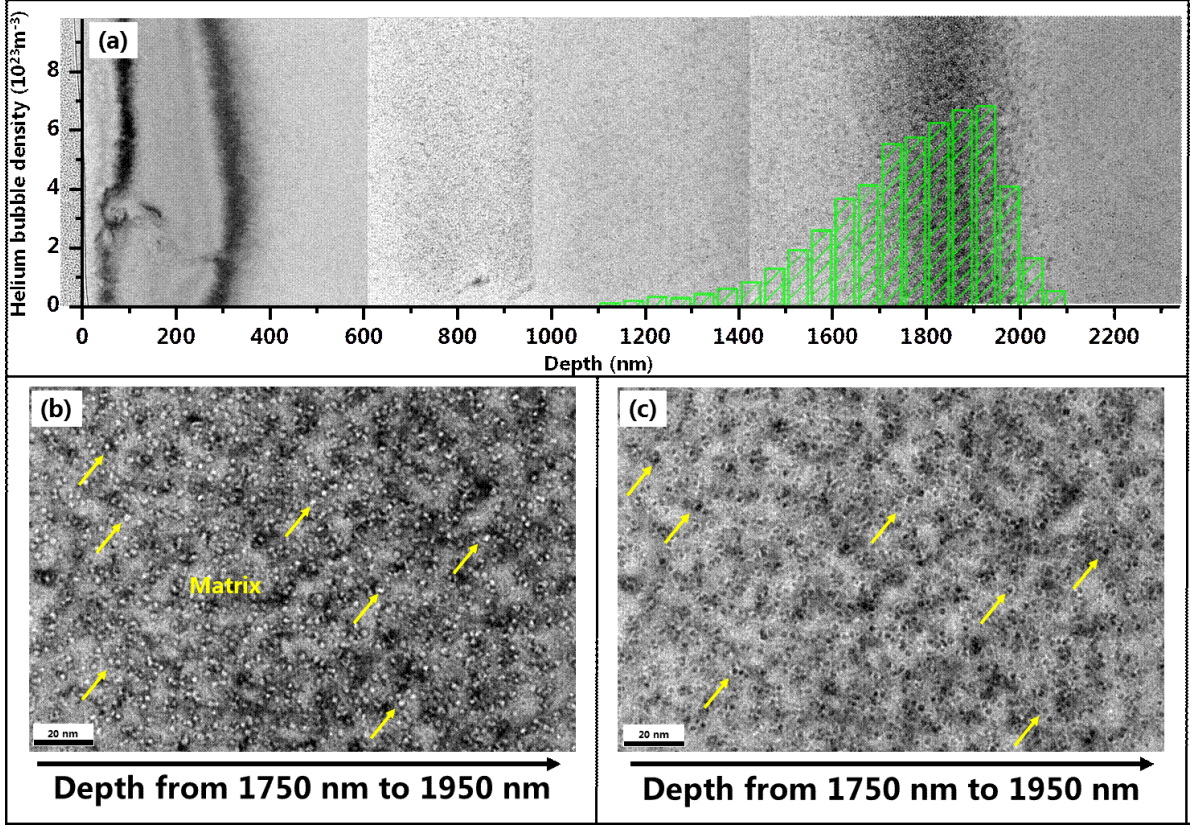


Fig. 5. (a) The bright-field TEM micrograph of the post-irradiated norm-GH3535 ($650\text{ }^{\circ}\text{C}$, 3×10^{16} ions/cm²). The magnified images of peak damage regions under (b) under-focus and (c) over-focus conditions.

Lastly, we estimated the internal He pressure in formed bubbles employing following equilibrium bubble pressure equation [34]:

$$P = \frac{2\gamma}{r}, \quad (2)$$

where γ is the surface energy ($\sim 2.0\text{ J/m}^2$ for nickel-based alloys). Here, a classical equation of state proposed by Mill [35], is used to calculate the bubble pressure at the peak damage region:

$$V_{molar} = \left(22.575 + 0.0064655T - 7.2645T^{-\frac{1}{2}}\right) * P^{-\frac{1}{3}} + (-12.483 - 0.024549T) * P^{-\frac{2}{3}} + \left(1.0596 + 0.10604T - 19.641T^{-\frac{1}{2}} + 189.84T^{-1}\right) * P^{-1}, \quad (3)$$

where T is the absolute temperature in Kelvin; P is the pressure in kilobars. The He bubbles are assumed to be in equilibrium state, the pressure in the nano-GH3535 samples under three different irradiation fluences is estimated to be 5.41, 4.04 and 3.65 GPa, respectively. The corresponding He-to-vacancy ratio in the bubbles is 1.26, 1.14 and 1.11. By using the molar volume and bubble density, the He concentration is also calculated, and the values are estimated to be ~ 0.14 , 0.35 and 0.62 at.%. It is worthy noted that calculated He concentration is much lower than the values predicted by SRIM simulation. This discrepancy indicates that there is a large number of small He bubbles, which were

not detected by TEM, or the He bubbles are more likely to be over pressurized [9]. Moreover, in norm-GH3535, this value is ~ 0.49 at.% in the case of ion fluence of 3×10^{16} ions/cm², which is higher than that in nano-GH3535 (0.35 at.%) under the same condition. This also means that fewer He atoms are contributed to the formation of observable He bubbles by TEM in nano-GH3535.

When comparing the He bubbles in norm-GH3535 and nano-GH3535, it became clear that the He bubbles in the nano-GH3535 are noticeably smaller while their density is higher. The smaller average size and higher number density can be explained as follow. In the case of nano-GH3535 microstructure, a large number of He atoms is trapped at the grain boundaries, this then reduces the He atoms supply for the growth of already nucleated He bubbles [29]. Hence, the mean size of He bubbles is smaller in nano-GH3535. A large number of interstitials can be absorbed preferentially by the grain boundaries in nano-GH3535 under irradiation, resulting in more vacancies being left behind, which can then form vacancy clusters, which provide more nuclear sites for even more He bubbles. These lead to the formation of large number of small He bubbles in the nano-grained microstructure. The formation of He bubbles causes swelling of the alloy, and its severity is mainly related to the volume fraction of formed He bubbles. In this study, the volume fraction of He bubbles in the nano-GH3535 irradiated with the ion fluence of 3×10^{16} ions/cm² was estimated to be 0.098%, while in the norm-GH3535 it was estimated to be about 0.145%. These results suggest the nano-GH3535 with nano-grained microstructure possess better He swelling resistance than the norm-GH3535 with fully-annealed coarse-grained microstructure. This can be of technological importance as the swelling of Ni-based alloys under operation conditions of a nuclear reactor can lead to premature failure of components and structures.

3.2 Effect of He bubbles on mechanical properties

In order to explore the effect of the He⁺ irradiation on the mechanical properties we performed a series of nano-indentation measurements. Figs. 6(a) and 6(b) shows the averaged nano-indentation measurements as a function of depth - i.e. distance from the irradiated surface (0 nm) of both nano-GH3535 and norm-GH3535 before and after He⁺ ion irradiation. Note that owing to the surface effect on the accuracy of the measurement, the nano-indentation measurements corresponding to a depth less than 70 nm are omitted. It becomes immediately apparent from nano-indentation measurements in Figs. 6(a) and 6(b) that the ion irradiation has a much great effect on the hardness of nano-grained microstructure than it has on fully-annealed coarse-grained microstructure. One, however, needs to be cautious when evaluation hardness of the crystalline material from the hardness depth-profile in particular when assessing the effect of the ion irradiation due the presence of so-called Indentation Size Effect (ISE), and Softer Substrate Effect (SSE).

Nix and Gao [36] introduced a model describing the ISE for crystalline materials based on geometrically necessary dislocations (GNDs), in which the depth dependence of the hardness can be expressed as follows:

$$H = H_0 \sqrt{1 + \frac{h^*}{h}}, \quad (4)$$

where, H is the measured hardness at the certain depth (h) of indentation, H_0 is the hardness at infinite depth, and h^* is the characteristic length that depends on the shape of the indenter tip, the shear modulus and H_0 . The obtained nano-indentation measurements are thus plotted as H^2 (y axis)

and $1/h$ (x axis) in Figs. 6(c) and 6(d). The unirradiated nano-indentation measurements basically follow a linear relationship as one would expect based on the Nix-Gao model (Eq. 4), however, the measurements taken on the ion-irradiated samples (regardless of the fluence or the grain size) does not follow a linear relationship predicted by the model. The hardness-depth profiles for irradiated specimens displays a rather clear bi-linear relation with the inflection point at depth of about 350 nm again regardless of the fluence or the grain size. It has been shown in Ref. [37] that this deviation from the linear Nix-Gao model is caused by the presence of the SSE – i.e. the plastic deformation of the softer unirradiated region (substrate) beyond the harder ion-irradiated near-surface region affects the hardness measurement. Note that unirradiated softer undelay will start to plasticity deform before the tip reaches that part of the material. The SSE, therefore, affects the hardness-depth profile while still probing hardened ion-irradiated region thus leading to a misleading hardness measurement. The inflection points in both Figs. 6(c) and 6(d) at 350 nm, which is about 1/6 of the irradiation damage layer depth (~2000 nm). This result is consistent well with the previous studies in Ref. [22, 38].

For unirradiated samples, the hardness H_0 calculated by fitting the hardness data at depth from 70 nm to 1200 nm, and the value was calculated as 7.46 GPa. As for the irradiated samples, the hardness at depth from 70 nm to 350 nm can be fitting to obtain the hardness at certain level of ion-induced damage. As the ion fluence increases, the nano-hardness of the irradiated nano-GH3535 samples was calculated respectively as 9.52, 9.62 and 9.78 GPa according to this depth interval. Moreover, the nano-hardness increments (ΔH) defined by the value difference of H_0 between the irradiated and unirradiated samples. According, the ΔH values for three irradiation cases are measured to be 2.06, 2.16 and 2.32 GPa. It is evident that the hardness increases with an increase in the irradiation dose. In the similar fashion, we have analyzed the nano-indentation measurements for the norm-GH3535 alloy's condition. By fitting the linear relationship into nano-indentation measurements in Fig. 6(d), The nano-hardness of norm-GH3535 samples under the same conditions as nano-GH3535 before and after irradiation was calculated as 2.77, 3.38, 3.74 and 3.88 GPa, and the ΔH values for three irradiation cases are measured to be 0.61, 0.97 and 1.11 GPa.

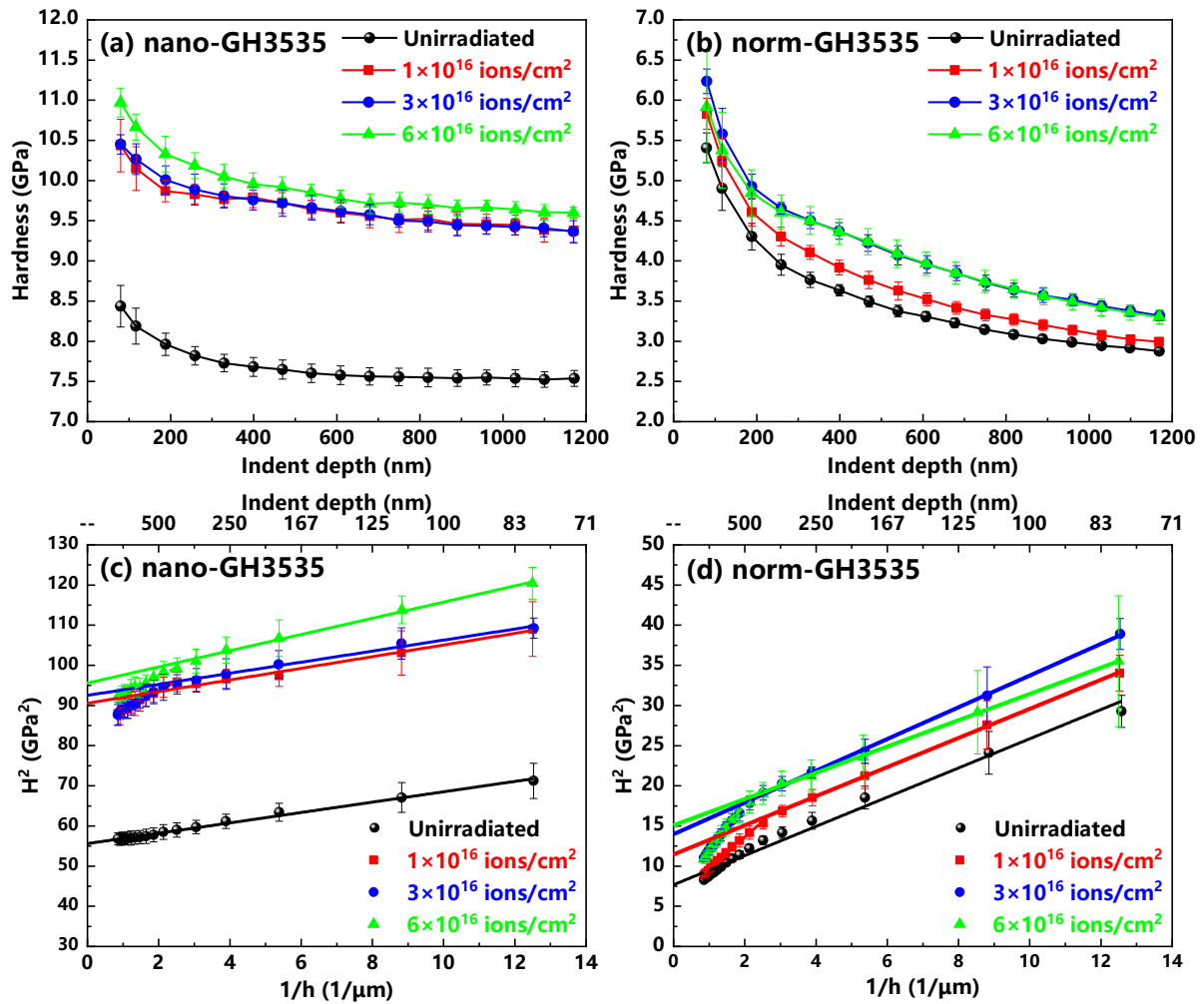


Fig. 6. The average nano-hardness measurements as a function of depth (distance from the irradiated surface) of both studied conditions before and after He⁺ ion irradiation are shown in (a) nano-GH3535 and for (c) norm-GH3535 and corresponding profiles of H^2 versus $1/h$ are shown in (b) and (d), respectively.

Fig. 7 presents the estimated hardness values of the ion-irradiated region versus the ion fluence in both nano-GH3535 and norm-GH3535. The irradiation induce hardening occurred in both alloys. Moreover, the hardness appears increasing continuously with the increase of fluence in norm-GH3535, while in the nano-GH3535 the hardness is increasing in a rather more incremental manner as a function of increasing fluence.

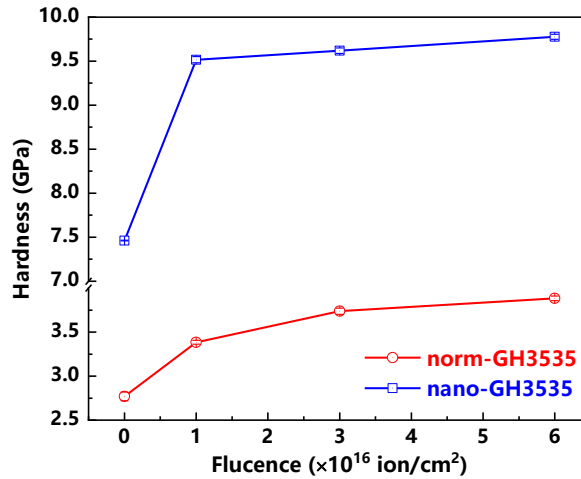


Fig. 7. The hardness of post-irradiated norm-GH3535 and nano-GH3535 versus ion fluence

The hardness of the unirradiated nano-GH3535 is about three times as much as the of the unirradiated norm-GH3535. As expected, this is caused by the Hall-Petch (grain-size) strengthening, which has a direct effect on the yield strength of the alloy. As for the irradiated samples, their irradiation induced hardening (hardness increase) is mainly caused by the presence of He bubbles and the severity depends directly on the volume fraction of He bubbles. In the case of ion fluence of 3×10^{16} ions/cm 2 , the volume fraction of He bubbles in nano-GH3535 is smaller than that in norm-GH3535. One would thus intuitively expect the hardness increase to be smaller for the nano-grained microstructure, however, it is clear from Figs. 6 and 7 that the increase in the hardness of the nano-GH3535 is more significant than in the norm-GH3535 under the same ion fluence. This suggests stronger irradiation-induced hardening of the nano-grained alloy comparing to coarse-grained alloy.

Companied with the ion irradiation, high temperature may lead to the microstructural changes in the HPT materials [39-42], which can affect the mechanical properties. Firstly, the grain-grown usually occur in the HPT materials at high temperature, which can result in a decrease of the hardness. However, as shown in Fig.8, the grain size remained practically unchanged after irradiation herein, which can be attributed partially to the large alloying element concentration [39-41]. Beside of the grain size, the density and arrangement of dislocation lines also has an influence on the hardness. Though the density of dislocation tends to reduce largely after annealing, according to previous studies [40, 41], the decrease of the mobile dislocation density can decrease the softening effect of reduced dislocation density. As a consequence, the microstructural changes induced by high temperature have no considerable effect on the hardness.

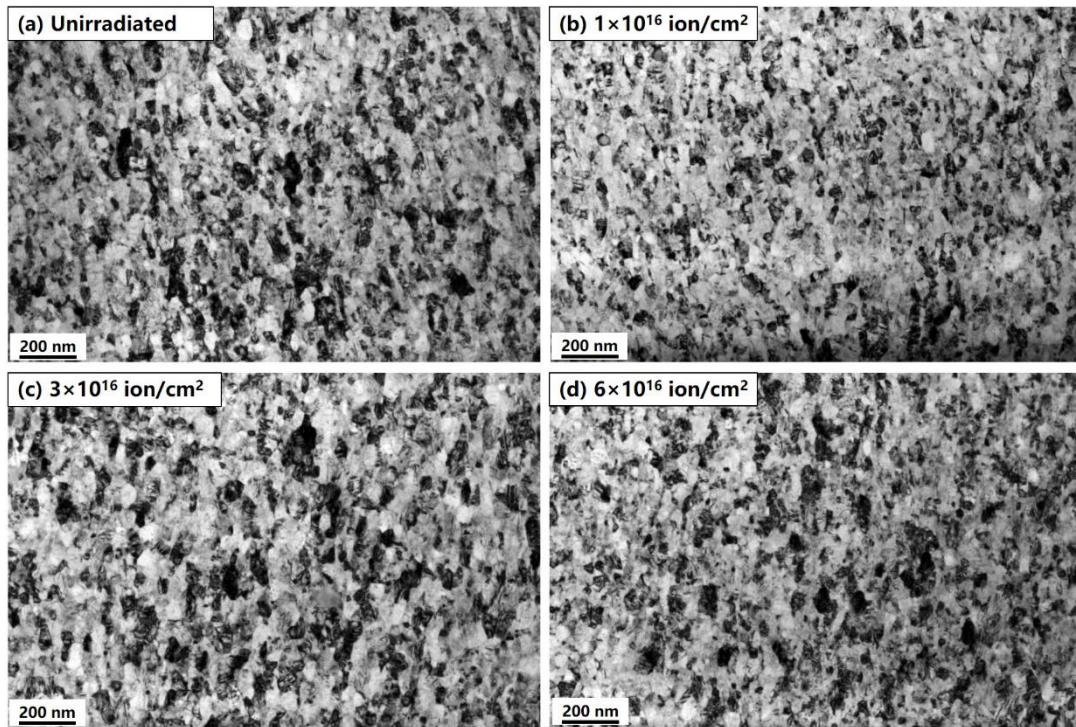


Fig.8 The bright-field TEM micrographs of unirradiated and post-irradiated nano-GH3535 condition

It is noted that defects introduced by irradiation may enhance the effect of high temperature in the microstructural changes. The helium atoms, aggregated at grain boundaries, may yield both kinetic and thermodynamic retardation of the grain growth as well. Interstitials can contribute to the climbing and disappearance of mobile dislocation [43], which result in less density of mobile dislocation density. These microstructural changes can lead to the increase of the hardness. Furthermore, According to MD studies [44, 45], the dislocations are emitted from grain boundaries and move across the grain during tension loading. The regions of high free volume in the grain boundaries or triple junctions can act as the preferential sites for emission of dislocations. He atoms, as similar as H atoms, preferentially aggregate and grow at the grain boundary and occupy the priority point of dislocation line emission to impede dislocation emission and the movement of dislocation lines between grains, thus lead to the hardening of alloy [45]. It should be noted that this impeding effect seems to be independent of the size and number density of He bubbles at the grain boundary, and the effect strength is far greater than that of the dispersed barrier hardening (DBH) of He bubbles in the grains [33]. Therefore, the irradiation induced hardness increase in nano-GH3535 is much larger than that of in norm-GH3535, rather than the influence of the volume fraction of He bubbles.

4. Conclusion

In summary, the both nano-GH3535 and norm-GH3535 alloys have been irradiated by He ion at 650 °C with ion fluence up to 6×10^{16} ions/cm². The He bubble formation is observed by TEM while the irradiation induced hardening is investigated using nano-indentation technique. The main conclusions are as follows:

(1) Nano-scaled He bubbles are observed in the nano-GH3535. With an increasing irradiation dose, both the average size and number density of He bubbles is increasing.

(2) Compared with the norm-GH3535, the He bubbles observed in the nano-GH3535 are smaller and denser. Additionally, the volume fraction of He bubbles is lower in the nano-GH3535. Hence, it is concluded that nano-grained microstructure could suppress the He swelling.

(3) These grain boundaries decorated with He bubbles will become stronger barriers to the movement of dislocation lines between grains, which leads to the much higher hardness increment in nano-GH3535 after irradiation than that of in norm-GH3535. This suggests stronger irradiation-induced hardening of the nano-grained alloy comparing to coarse-grained alloy.

Acknowledgments

This work was supported by the National Natural Science Foundation of China (Grant No. 11975304).

References

- [1] J. Serp, M. Allibert, O. Benes, S. Delpech, O. Feynberg, V. Ghetta, D. Heuer, D. Holcomb, V. Ignatiev, J.L. Kloosterman, L. Luzzi, E. Merle-Lucotte, J. Uhlir, R. Yoshioka, Z.M. Dai, The molten salt reactor (MSR) in generation IV: Overview and perspectives, *Prog. Nucl. Energ.* 77 (2014) 308-319.
- [2] D. LeBlanc, Molten salt reactors: A new beginning for an old idea, *Nucl. Eng. Des.* 240 (2010) 1644-1656.
- [3] Z.B. Zhu, H.F. Huang, J.Z. Liu, J. Gao, Z.Y. Zhu, Xenon ion irradiation induced hardening in inconel 617 containing experiment and numerical calculation, *J. Nucl. Mater.* 525 (2019) 32-39.
- [4] V. Ignatiev, Molten Salts for Safe, Low Waste and Proliferation Resistant Treatment of Radwaste in Accelerator Driven and Critical Systems, *Molten Salts: From Fundamentals to Applications*, Springer2002, pp. 263-282.
- [5] M. Figueroa, Preliminary Fluoride Salt-Cooled High Temperature Reactor (FHR) Materials and Components White Paper, Department of Nuclear Engineering, University of California Berkeley (2012).
- [6] C. Du, S. Jin, Y. Fang, J. Li, S. Hu, T. Yang, Y. Zhang, J. Huang, G. Sha, Y. Wang, Ultrastrong steel with exceptional thermal stability and radiation tolerance, *Nat. Commun.* 9 (2018) 1-9.
- [7] L.L. Hsiung, M.J. Fluss, S.J. Tumey, B.W. Choi, Y. Serruys, F. Willaime, A. Kimura, Formation mechanism and the role of nanoparticles in Fe-Cr ODS steels developed for radiation tolerance, *Phys. Rev. B* 82 (2010) 184103.
- [8] W.Z. Han, M.J. Demkowicz, E.G. Fu, Y.Q. Wang, A. Misra, Effect of grain boundary character on sink efficiency, *Acta Mater.* 60 (2012) 6341-6351.
- [9] Z. Shang, J. Ding, C. Fan, D. Chen, J. Li, Y. Zhang, Y. Wang, H. Wang, X. Zhang, He ion irradiation response of a gradient T91 steel, *Acta Mater.* 196 (2020) 175-190.
- [10] O. El-Atwani, J.E. Nathaniel, A.C. Leff, B.R. Muntifering, J.K. Baldwin, K. Hattar, M.L. Taheri, The role of grain size in He bubble formation: Implications for swelling resistance, *J. Nucl. Mater.* 484 (2017) 236-244.
- [11] O. El-Atwani, J.A. Hinks, G. Greaves, J.P. Allain, S.A. Maloy, Grain size threshold for enhanced irradiation resistance in nanocrystalline and ultrafine tungsten, *Mater. Res. Lett.* 5 (2017) 343-349.
- [12] C.M. Barr, N. Li, B.L. Boyce, K. Hattar, Examining the influence of grain size on radiation

- tolerance in the nanocrystalline regime, *Appl. Phys. Lett.* 112 (2018) 181903.
- [13] W. Han, E.G. Fu, M.J. Demkowicz, Y. Wang, A. Misra, Irradiation damage of single crystal, coarse-grained, and nanograined copper under helium bombardment at 450 °C, *J. Mater. Res.* 28 (2013) 2763-2770.
- [14] G.R. Odette, P. Miao, D.J. Edwards, T. Yamamoto, R.J. Kurtz, H. Tanigawa, helium transport, fate and management in nanostructured ferritic alloys: In situ helium implantation studies, *J. Nucl. Mater.* 417 (2011) 1001-1004.
- [15] B.N. Singh, A.J.E. Foreman, Calculated grain size-dependent vacancy supersaturation and its effect on void formation, *Philos. Mag.* 29 (2006) 847-858.
- [16] M. Samaras, P.M. Derlet, H. Van Swygenhoven, M. Victoria, Radiation damage near grain boundaries, *Philos. Mag.* 83 (2003) 3599-3607.
- [17] M. Umemoto, Nanocrystallization of Steels by Severe Plastic Deformation, *Mater. Trans.* 44 (2003) 1900-1911.
- [18] R. Valiev, Nanostructuring of metals by severe plastic deformation for advanced properties, *Nat. Mater.* 3 (2004) 511-516.
- [19] J. Wang, X. Gao, N. Gao, Z.G. Wang, M.H. Cui, K.F. Wei, C.F. Yao, J.R. Sun, B.S. Li, Y.B. Zhu, L.L. Pang, Y.F. Li, D. Wang, E.Q. Xie, Grain size effects on He bubbles distribution and evolution, *J. Nucl. Mater.* 457 (2015) 182-185.
- [20] K.Y. Yu, Y. Liu, C. Sun, H. Wang, L. Shao, E.G. Fu, X. Zhang, Radiation damage in helium ion irradiated nanocrystalline Fe, *J. Nucl. Mater.* 425 (2012) 140-146.
- [21] J. Lv, Effect of grain size on mechanical property and corrosion resistance of the Ni-based alloy 690, *J. Mater. Sci. Technol.* 34 (2018) 1685-1691.
- [22] H.F. Huang, J. Gao, B. Radigue, R.D. Liu, J.J. Li, G.H. Lei, Q. Huang, M. Liu, R.B. Xie, Microstructural evolution and hardening of GH3535 alloy under energetic Xe ion irradiation at room temperature and 650 °C, *J. Nucl. Mater.* 499 (2018) 431-439.
- [23] C. Fan, Q. Li, J. Ding, Y. Liang, Z. Shang, J. Li, R. Su, J. Cho, D. Chen, Y. Wang, J. Wang, H. Wang, X. Zhang, helium irradiation induced ultra-high strength nanotwinned Cu with nanovoids, *Acta Mater.* 177 (2019) 107-120.
- [24] J.F. Ziegler, J.P. Biersack, SRIM – The stopping and range of ions in matter, *Treatise on heavy-ion science*, Springer 1985, pp. 93-129.
- [25] S.J. Zinkle, B.N. Singh, Analysis of displacement damage and defect production under cascade damage conditions, *J. Nucl. Mater.* 199(3) (1993) 173-191.
- [26] L.K. Béland, C.Y. Lu, Y.N. Osetskiy, G.D. Samolyuk, A. Caro, L.M. Wang, R.E. Stoller, Features of primary damage by high energy displacement cascades in concentrated Ni-based alloys, *J. Appl. Phys.* 119 (2016) 085901.
- [27] G.B. Shan, Y.Z. Chen, N.N. Liang, H. Dong, W.X. Zhang, T. Suo, F. Liu, Irradiation resistance of a thermally stable nanocrystalline Fe-1 at.% Zr alloy, *Mater. Lett.* 238 (2019) 261-263.
- [28] G.S. Was, *Fundamentals of radiation materials science: metals and alloys*, Springer, 2016.
- [29] H.F. Huang, W. Zhang, M. De Los Reyes, X.L. Zhou, C. Yang, R. Xie, X.T. Zhou, P. Huai, H.J. Xu, Mitigation of He embrittlement and swelling in nickel by dispersed SiC nanoparticles, *Mater. Design* 90 (2016) 359-363.
- [30] J.Z. Liu, H.F. Huang, J. Gao, Z.B. Zhu, Y. Li, Defects evolution and hardening in the Hastelloy N

- alloy by subsequent Xe and He ions irradiation, *J. Nucl. Mater.* 517 (2019) 328-336.
- [31] J.Z. Liu, H.F. Huang, R.D. Liu, Z.B. Zhu, Q.T. Lei, A.W. Liu, Y. Li, In situ TEM observation of the evolution of helium bubbles in Hastelloy N alloy during annealing, *J. Nucl. Mater.* 537 (2020) 152184.
- [32] Y. Lu, H.F. Huang, X. Gao, C. Ren, J. Gao, H. Zhang, S. Zheng, Q. Jin, Y. Zhao, C. Lu, T. Wang, T. Li, A promising new class of irradiation tolerant materials: Ti₂ZrHfV_{0.5}Mo_{0.2} high-entropy alloy, *J. Mater. Sci. Technol.* 35 (2019) 369-373.
- [33] Z.B. Zhu, H.F. Huang, J.Z. Liu, Z.Y. Zhu, helium-induced damage behavior in high temperature nickel-based alloys with different chemical composition, *J. Nucl. Mater.* 541 (2020) 152419.
- [34] H. Trinkaus, B.N. Singh, helium accumulation in metals during irradiation – where do we stand?, *J. Nucl. Mater.* 323 (2003) 229-242.
- [35] R.L. Mills, D.H. Liebenberg, J.C. Bronson, Equation of state and melting properties of He₄ from measurements to 20 kbar, *Phys. Rev. B* 21 (1980) 5137-5148.
- [36] W.D. Nix, H.J. Gao, Indentation size effects in crystalline materials: A law for strain gradient plasticity, *J. Mech. Phys. Solids.* 46 (1998) 411-425.
- [37] R. Kasada, Y. Takayama, K. Yabuuchi, A. Kimura, A new approach to evaluate irradiation hardening of ion-irradiated ferritic alloys by nano-indentation techniques, *Fusion. Eng. Des.* 86 (2011) 2658-2661.
- [38] H.F. Huang, J.J. Li, D.H. Li, R.D. Liu, G.H. Lei, Q. Huang, L. Yan, TEM, XRD and nanoindentation characterization of Xenon ion irradiation damage in austenitic stainless steels, *J. Nucl. Mater.* 454 (2014) 168-172.
- [39] G. Kapoor, Y. Huang, V.S. Sarma, T.G. Langdon, J. Gubicza, Evolution of the microstructure during annealing of ultrafine-grained Ni with different Mo contents, *Mater. Charact.* 130 (2017) 56-63.
- [40] G. Kapoor, Y. Huang, V.S. Sarma, T.G. Langdon, J. Gubicza, Influence of Mo alloying on the thermal stability and hardness of ultrafine-grained Ni processed by high-pressure torsion, *J. Mater. Res. Technol.* 6 (2017) 361-368.
- [41] M. El-Tahawy, P.H.R. Pereira, Y. Huang, H. Park, H. Choe, T.G. Langdon, J. Gubicza, Exceptionally high strength and good ductility in an ultrafine-grained 316L steel processed by severe plastic deformation and subsequent annealing, *Mater. Lett.* 214 (2018) 240-242.
- [42] M. El-Tahawy, Y. Huang, H. Choi, H. Choe, J.L. Labar, T.G. Langdon, J. Gubicza, High temperature thermal stability of nanocrystalline 316L stainless steel processed by high-pressure torsion, *Mat. Sci. Eng. A* 682 (2016) 323-331.
- [43] H.C. Chen, D.H. Li, R.D. Liu, H.F. Huang, J.J. Li, G.H. Lei, Q. Huang, L.M. Bao, L. Yan, X.T. Zhou, Z.Y. Zhu, Ion irradiation induced disappearance of dislocations in a nickel-based alloy, *Nucl. Instrum. Meth. B* 377 (2016) 94-98.
- [44] D. Farkas, L. Patrick, Tensile deformation of fcc Ni as described by an EAM potential, *Philips. Mag.* 89 (2009) 3435-3450.
- [45] B. Kuhr, D. Farkas, I.M. Robertson, Atomistic studies of hydrogen effects on grain boundary

structure and deformation response in FCC Ni, *Comp. Mater. Sci.* 122 (2016) 92-101.